

Thermoelectric enhancement in triple-doped strontiumtitanate with multi-scale microstructure

Zheng Cao(曹正), Qing-Qiao Fu(傅晴俏), Hui Gu(顾辉), Zhen Tian(田震), Xinba Yaer(新巴雅尔), Juan-Juan Xing(邢娟娟), Lei Miao(苗蕾), Xiao-Huan Wang(王晓欢), Hui-Min Liu(刘慧敏), and Jun Wang(王俊)
Citation: Chin. Phys. B, 2021, 30 (**9**): 097204. DOI: 10.1088/1674-1056/abe9a9
Journal homepage: http://cpb.iphy.ac.cn; http://iopscience.iop.org/cpb

What follows is a list of articles you may be interested in

First principles calculations on the thermoelectric properties of bulk Au_2S with ultra-low lattice thermal conductivity

Y Y Wu(伍义远), X L Zhu(朱雪良), H Y Yang(杨恒玉), Z G Wang(王志光), Y H Li(李玉红), B T Wang(王保田)
Chin. Phys. B, 2020, 29 (**8**): 087202. DOI: 10.1088/1674-1056/ab973c

Electrically tunable spin diode effect in a tunneling junction of quantum dot

Xukai Peng(彭许凯), Zhengzhong Zhang(张正中)
Chin. Phys. B, 2019, 28 (**12**): 127202. DOI: 10.1088/1674-1056/ab53d0

The magneto-thermoelectric effect of graphene with intra-valley scattering

Wenye Duan(段文晔), Junfeng Liu(刘军丰), Chao Zhang(张潮), Zhongshui Ma(马中水)
Chin. Phys. B, 2018, 27 (**9**): 097204. DOI: 10.1088/1674-1056/27/9/097204

Complex alloying effect on thermoelectric transport properties of $Cu_2Ge(Se_{1-x}Te_x)_3$

Ruifeng Wang(王瑞峰), Lu Dai(戴璐), Yanci Yan(闫艳慈), Kunling Peng(彭坤岭), Xu Lu(卢旭), Xiaoyuan Zhou(周小元), Guoyu Wang(王国玉)
Chin. Phys. B, 2018, 27 (**6**): 067201. DOI: 10.1088/1674-1056/27/6/067201

Thermoelectric properties of lower concentration K-doped $Ca_3Co_4O_9$ ceramics

Ya-Nan Li(李亚男), Ping Wu(吴平), Shi-Ping Zhang(张师平), Sen Chen(陈森), Dan Yan(闫丹), Jin-GuangYang(杨金光), Li Wang(王立), Xiu-Lan Huai(淮秀兰)
Chin. Phys. B, 2018, 27 (**5**): 057201. DOI: 10.1088/1674-1056/27/5/057201

Thermoelectric enhancement in triple-doped strontium titanate with multi-scale microstructure*

Zheng Cao(曹正)[1,†], Qing-Qiao Fu(傅晴俏)[2,†], Hui Gu(顾辉)[2], Zhen Tian(田震)[1], Xinba Yaer(新巴雅尔)[1], Juan-Juan Xing(邢娟娟)[2,‡], Lei Miao(苗蕾)[3], Xiao-Huan Wang(王晓欢)[1], Hui-Min Liu(刘慧敏)[1], and Jun Wang(王俊)[1,§]

[1] *Inner Mongolia Engineering Research Center of Multi-functioanl Copper Based Materials, School of Materials Science and Engineering, Inner Mongolia University of Technology, Hohhot* 010051, *China*

[2] *School of Materials Science and Engineering, Materials Genome Institute, Shanghai University, Shanghai* 200444, *China*

[3] *School of Material Science and Engineering, Guilin University of Electronic Technology, Guilin* 541004, *China*

(Received 27 January 2021; revised manuscript received 15 February 2021; accepted manuscript online 25 February 2021)

Strontium titanate ($SrTiO_3$) is a thermoelectric material with large Seebeck coefficient that has potential applications in high-temperature power generators. To simultaneously achieve a low thermal conductivity and high electrical conductivity, polycrystalline $SrTiO_3$ with a multi-scale architecture was designed by the co-doping with lanthanum, cerium, and niobium. High-quality nano-powders were synthesized via a hydrothermal method. Nano-inclusions and a nano/micro-sized second phase precipitated during sintering to form mosaic crystal-like and epitaxial-like structures, which decreased the thermal conductivity. Substituting trivalent Ce and/or La with divalent Sr and substituting pentavalent Nb with tetravalent Ti enhanced the electrical conductivity without decreasing the Seebeck coefficient. By optimizing the dopant type and ratio, a low thermal conductivity of 2.77 $W{\cdot}m^{-1}{\cdot}K^{-1}$ and high PF of 1.1 $mW{\cdot}m^{-1}{\cdot}K^{-2}$ at 1000 K were obtained in the sample co-doped with 5-mol% La, 5-mol% Ce, and 5-mol% Nb, which induced a large ZT of 0.38 at 1000 K.

Keywords: strontium titanate, multiple-doping, multi-scale microstructure, nano-inclusions

PACS: 72.15.Jf, 84.60.Rb, 77.84.Cg, 81.20.−n **DOI:** 10.1088/1674-1056/abe9a9

1. Introduction

Strontium titanate ($SrTiO_3$) is a promising thermoelectric material for applications in electricity generation and sensors like photothermoelectric devices[1] because of its high stability and large Seebeck coefficient (S).[2] A large S and electrical conductivity (σ) and a low thermal conductivity (κ) are needed to obtain a high thermoelectric dimensionless figure of merit, $ZT = S^2\sigma T/\kappa$.[3] It is expected that a high ZT of $SrTiO_3$ can be obtained by reducing κ and increasing $PF = S^2\sigma$;[4] however, the interdependence of S, σ, and κ complicates control of the thermal electrical transport properties of bulk materials.[5] The ZT of many alloys and inorganic compounds has been improved by separately controlling S, σ, and κ through band-engineering,[6] component control,[7–9] and structure control.[10–12] Some layer-structured oxides[13,14] and two-dimensional $SrTiO_3$[15,16] exhibit high ZT values because of their intrinsically low thermal conductivity or large PF. $SrTiO_3$ thin films with a high ZT have been obtained, but polycrystalline bulk materials are more suitable for thermoelectric applications. The ZT of polycrystalline $SrTiO_3$ still falls short of requirements due to its high thermal conductivity and low carrier mobility. The σ of $SrTiO_3$ can be optimized by doping to increase the carrier concentration.[17–24]

Combining heavy doping and compositing allows the coordinated control of electrical conductivity and thermal conductivity.[25,26] Previous works have shown that La and Nb are effective n-type dopants that can enhance electrical transport properties when used to replace Sr and Ti, respectively.[17,26] But the thermal conductivity of $SrTiO_3$ is still higher than other perovskite oxides such as $SrCeO_3$ and $BaCeO_3$.[27] If Ce reduces the thermal conductivity, an improved ZT can be expected when Ce, La, and Nb are used to co-dope $SrTiO_3$ while maintaining a high power factor; however, there have been few reports on triple-doped $SrTiO_3$ thermoelectric materials. In this work, we introduce a high-performance La–Ce–Nb-doped $SrTiO_3$ thermoelectric with a low thermal conductivity and a relatively large power factor.

2. Experimental materials and methods

2.1. Sample preparation

$Sr_{1-x-y}La_xCe_yTi_{1-z}Nb_zO_3$ (x = 0–0.05, y = 0–0.05, z = 0–0.05) nanoparticles were prepared by a hydrothermal method. $NbCl_5$ (Shanghai Macklin Biochemical Co., Ltd.) was added into a mixture of ethylene glycol (Tianjin Fengchuan Chemical Reagent Co., Ltd.) and deionized water with a volume ratio of 1:1 and 10% [Ti(OBu)4] (Aladdin

*Project supported by the National Natural Science Foundation of China (Grant Nos. 51702168 and 51532006).

†These authors contributed equally.

‡Corresponding author. E-mail: xingjuanjuan@shu.edu.cn

§Corresponding author. E-mail: wangjun@imut.edu.cn

© 2021 Chinese Physical Society and IOP Publishing Ltd

Industrial Corporation) and mixed via ultrasonic oscillation. An aqueous solution containing 0.6 M $Sr(NO_3)_2$ and stoichiometric amounts of $Ce(NO_3)_3{\cdot}6H_2O$ and $La(NO_3)_3{\cdot}6H_2O$ (Aladdin Industrial Corporation) were added into the above solution, followed by the addition of 6.4 M NaOH (Aladdin Industrial Corporation). The obtained solution was immediately transferred to a 100 mL teflon-lined stainless-steel autoclave and held at 180 °C for 24 hours. The obtained powders were washed several times with glacial acetic acid to remove residual organic matter and then dried for 2 hours at 80 °C. The obtained nanoparticles were pre-pressed under 4.3 MPa using a hydraulic press, followed by cold isostatic pressing (CIP) under 200 MPa. The samples were then embedded into carbon powders and sintered at 1573 K for 5 hours in a muffle furnace to obtain a black bulk sample, as shown in the process schematic in Fig. 1.

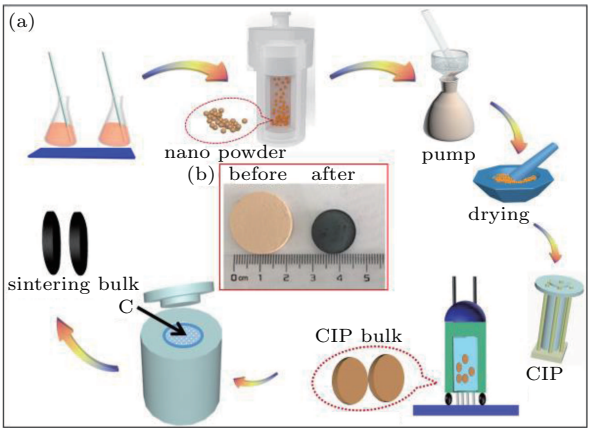


Fig. 1. The formation process of La–Ce–Nb-doped $SrTiO_3$. (a) Schematic diagram of the preparation method and (b) photos of obtained bulk samples before and after sintering.

2.2. Sample characterization

All specimens were characterized by scanning electron microscopy (SEM, Zeiss, G300), x-ray diffraction (XRD, Rigaku D/Max-2500), and transmission electron microscopy (TEM, JEOL F200). The electrical conductivity and Seebeck coefficient were measured from 300 K to 1000 K in a helium atmosphere using a Linseis LSR-3. Thermal conductivity (κ) was calculated by the equation $\kappa = DC_p\rho$, where the thermal diffusivity D was measured by the laser flash method using a NETZSCH LFA 457, the specific heat C_p was measured by differential scanning calorimetry using a NETZSCH DSC STA 449F3, and the density ρ was measured by Archimedes method. The Hall coefficients were measured using the van der Pauw method under a reversible magnetic field of 1.5 T.

3. Results and discussion

3.1. Phase analysis

Figure 2 shows the XRD and TEM images of La–Ce–Nb-doped powders. All $SrTiO_3$ powders doped with different dopants and doping ratios showed cubic perovskite structures (PDF#73-0661), and no impurity phase peaks were observed in the XRD patterns in Fig. 2(a) and the TEM-EDS result in Fig. 2(b). A slight broadening of the diffraction peak in Fig. 2(a) indicated that the powders had a small grain size, and the grain size distributed in 15 nm–40 nm, as determined from the TEM image (Fig. 2(c)). The distance between the two lattice stripes determined from the HRTEM image was 0.278 nm as shown in Fig. 2(d), which was consistent with the (110) planar spacing of $SrTiO_3$ (PDF#73-0661). The XRD

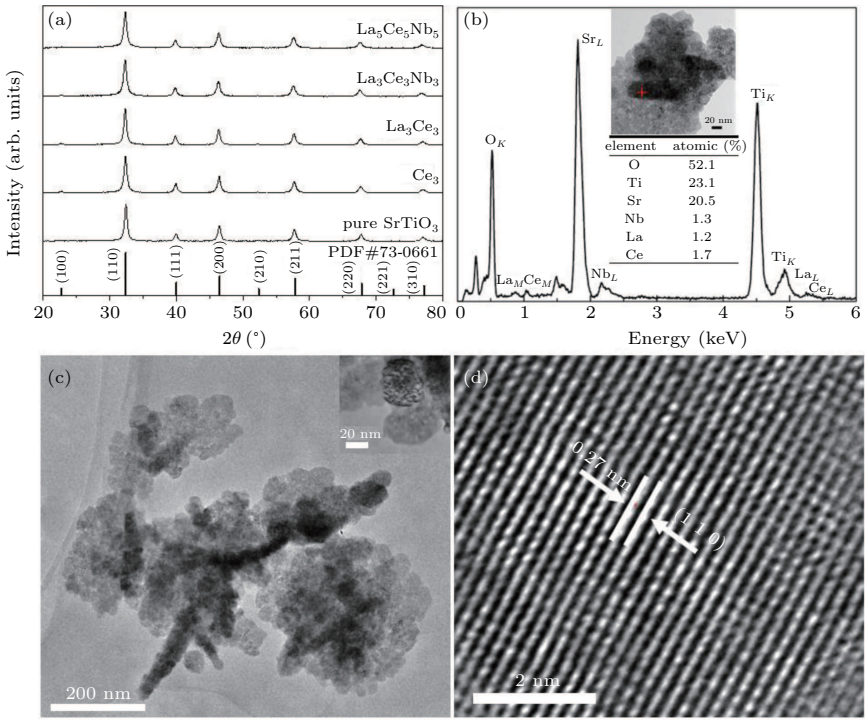


Fig. 2. (a) XRD patterns of La, Ce, and Nb co-doped $SrTiO_3$ powders with different doping ratios, (b) TEM-EDS, (c) TEM image and (d) HRTEM image of $La_5Ce_5Nb_5$ powder.

peaks shifted by different degrees as the doping concentration changed, due to the substitution of large Sr^{2+} (144.0 pm) ions at the A-site by smaller La^{3+} (136.0 pm) ions and Ce^{3+} (134.0 pm), as well as the substitution of small Ti^{4+} (60.5 pm) ions at B-site by larger Nb^{5+} (64.0 pm) ions. Moreover, the TEM-EDS analysis showed that La, Ce, and Nb were detected in $SrTiO_3$ grains for $La_5Ce_5Nb_5$, indicating the introduction of dopant elements into the $SrTiO_3$ lattice.

As shown in Fig. 3, the XRD patterns of bulk samples contained peaks attributed to a secondary phase, along with peaks for the $SrTiO_3$ main phase; however, the weak peaks did not match those in the standard XRD pattern, suggesting that the weak peaks appeared due to several kinds of secondary phases. The grains of all samples grew into irregular polyhedrons after sintering, as shown in Fig. 4.

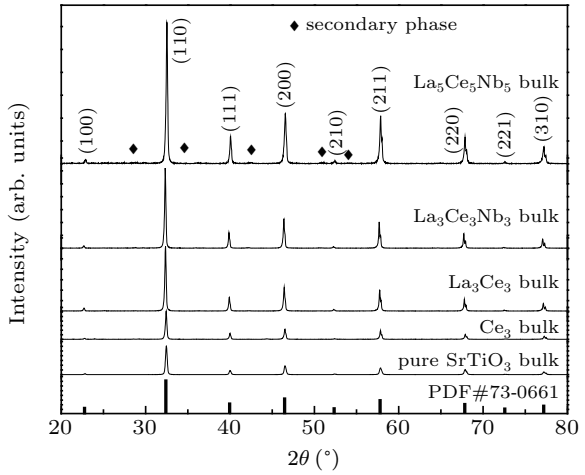


Fig. 3. XRD patterns of bulk $SrTiO_3$ samples with different La, Ce, and Nb ratios.

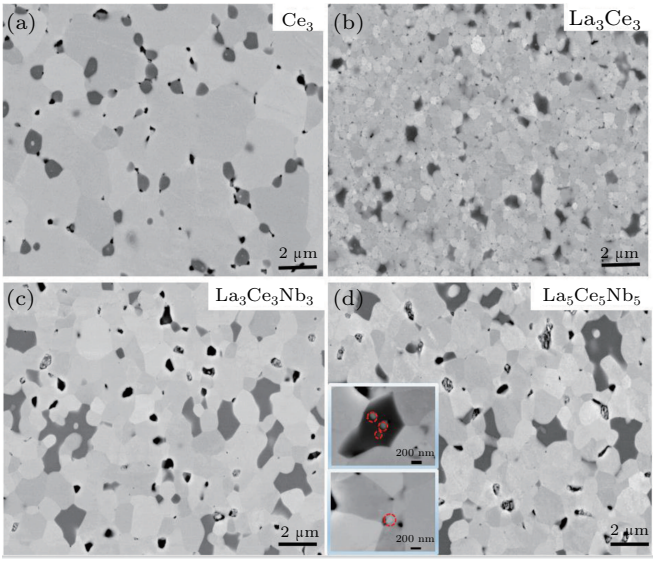


Fig. 4. SEM images of samples (a) Ce_3, (b) La_3Ce_3, (c) $La_3Ce_3Nb_3$, and (d) $La_5Ce_5Nb_5$ and the inset of the nano-inclusions and nano-scale grain.

3.2. Microstructural analysis

The bulk samples were compacted with relatively high densities as shown in Fig. 4, even though several types of grains with different contrasts, shapes, and sizes were observed. Many regular and gray grains were $SrTiO_3$, while the irregular and black grains, randomly distributed in the perovskite matrix were secondary phases. Furthermore, nanoparticles were observed in some secondary phase grains, and some of these particles were completely wrapped in the secondary phases, while the others were only partially wrapped. The grain sizes ranged from the nanoscale to the microscale except for the sample La_3Ce_3.

Figures 5(a) and 5(b) showed the SEM images and corresponding EDS element maps of $La_3Ce_3Nb_3$ and $La_5Ce_5Nb_5$, which showed that La, Ce, Nb, Sr, Ti, and O were evenly distributed in the matrix. Some Ti-rich oxide phase was observed, suggesting that the $SrTiO_3$ matrix partially decomposed during sintering. Figure 5(c) shows that La and Ce existed only in the matrix, and Nb was distributed both in the matrix and secondary phase, but there was more in the matrix than in the secondary phase.

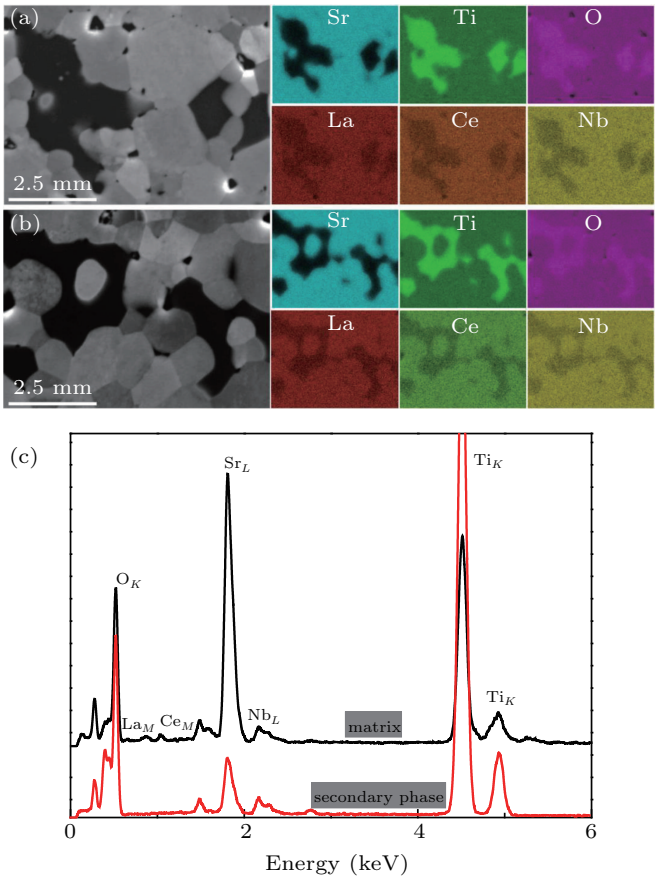


Fig. 5. The SEM images and EDS element maps of (a) $La_3Ce_3Nb_3$ and (b) $La_5Ce_5Nb_5$, and (c) EDS analysis of $La_5Ce_5Nb_5$.

The electron back-scatter diffraction (EBSD) analysis showed that a large amount of Ti–O secondary phase was not TiO_2 and was in-homogeneously distributed in the $SrTiO_3$ polycrystalline matrix (Fig. 6). The HRTEM and selected electron diffraction pattern (SAED) pattern analysis (Fig. 7) indicated that these secondary phases were Ti_nO_{2n-1}. The

formation of the Ti_nO_{2n-1} phase likely formed due to mixed-valence titanium cations already in the powder and the oxygen vacancies generated in a reducing atmosphere, which partially transformed Ti^{4+} into Ti^{3+}.[28] Interestingly, some nano/microscale $SrTiO_3$ and Ti_nO_{2n-1} grains were included in each other's large grains, as shown in Fig. 7.

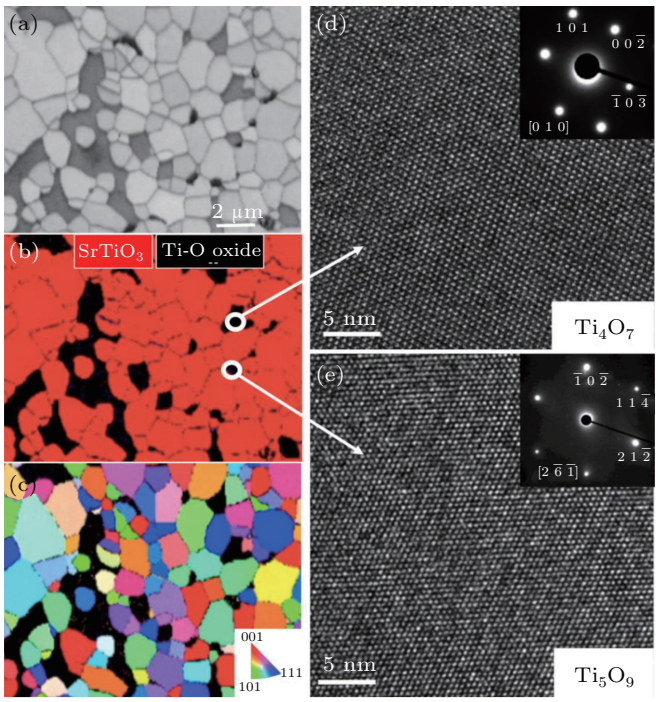


Fig. 6. Microstructural analysis of $La_5Ce_5Nb_5$ bulk sample: (a) electron back-scatter diffraction (EBSD) image, (b) phase mapping, (c) inverse pole figure (IPF) maps, and (d)–(e) HRTEM images of the secondary phases.

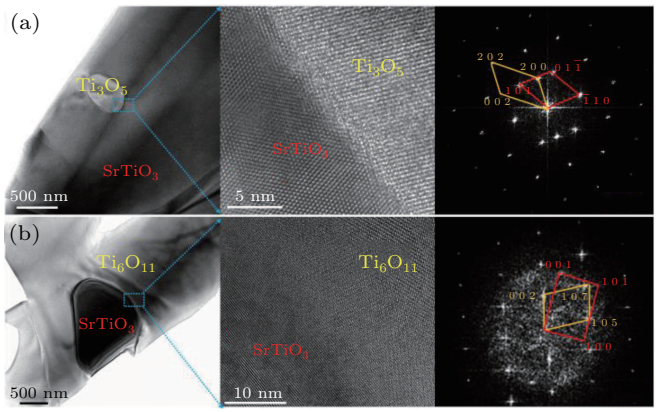


Fig. 7. Low and high resolution TEM images, and SAED pattern of $Ti_nO_{2n-1}/SrTiO_3$ interfaces. (a) $SrTiO_3$ grain with Ti_nO_{2n-1} inclusions, (b) Ti_nO_{2n-1} grain with $SrTiO_3$ inclusions.

The SAED patterns show that the [2 0 2] of Ti_nO_{2n-1} inclusions and [1 0 –1] of host $SrTiO_3$ grains have the same orientation, showing a coherent relationship (Fig. 7(a)), to form an epitaxial-like heterostructure, which reduced the thermal conductivity due to phonon scattering at the interface without reducing the electrical conductivity.[29–31] In addition, the $SrTiO_3$ inclusions smoothly connected with the Ti_nO_{2n-1} host grains (Fig. 7(b)), which also contributed to the phonon scattering with less electron scattering.

3.3. Electrical and thermal transport properties

The measured electrical transport properties as a function of temperature are shown in Fig. 8. The electrical conductivity increased until 420 K–470 K and then began to decrease above this temperature range, consistent with Nb-doped and La–Nb co-doped samples.[17,32,33] The lowest electrical conductivity of 23 $S{\cdot}cm^{-1}$ in sample Ce_3 was obtained at 1000 K, which increased upon increasing the dopant concentration to 247 $S{\cdot}cm^{-1}$ in sample $La_5Ce_5Nb_5$. This again indicated successful lattice doping. The electrical conductivity of a material can be estimated by the formula $\sigma = ne\mu$, where n, e, and μ are the carrier concentration, electronic charge, and carrier mobility, respectively. The Hall carrier concentrations of all samples were constant over the entire measured temperature range, indicating that all free electrons were injected into the conduction band, and no thermal activation of intrinsic carriers occurred within this temperature range.

The mobilities of all samples showed a temperature dependence that was similar to the electrical conductivity, which increased with temperature up to 400 K–450 K and then decreased above this temperature. These trends are related to the dominant scattering of ionized impurities and phonons at low and high temperatures, respectively.[26] The sample mobility increased with increasing carrier concentration, which is consistent with the grain size trend. Usually, the carrier mobility (μ), which is determined by the effective mass (m^*), and relaxation time (τ), is proportional to the electron mean free pass (l), are expressed as follows:

$$\mu = e\tau/m^*, \tag{1}$$

$$l = 2\tau\sqrt{\frac{3k_BT}{m^*}}, \tag{2}$$

where k_B, T, and e are the Boltzmann constant, absolute temperature, and electron charge, respectively.[34] The reduced effective mass and increased grain size at higher doping concentrations increased the electron mean free path, which is expected to enhance the mobility, resulting in a large σ in $La_5Ce_5Nb_5$.

Since the second phase was a Magneli-phase, which has a high electrical conductivity,[35–37] the higher amount of second phase did not significantly affect the electrical conductivity of $La_3Ce_3Nb_3$ and $La_5Ce_5Nb_5$. The mosaic crystal structure and the epitaxial-like relationship between nano/microscale inclusions and the corresponding host grain also contributed to the electronic transitions at interfaces.[38]

Figure 9(a) shows the temperature dependence of the Seebeck coefficient. A maximum Seebeck coefficient of 344 $\mu V{\cdot}K^{-1}$ was obtained in Ce_3, which decreased to 207 $\mu V{\cdot}K^{-1}$ at 1000 K upon increasing doping concentration in $La_5Ce_5Nb_5$. As shown in Fig. 9(b), in contrast with the electrical conductivity, the Seebeck coefficient decreased

upon increasing the dopant concentration, suggesting that $|S|$ decreased as n increased. This trend complies with the relationship between S and n,

$$S = \frac{8\pi^2 k_B^2}{3eh^2} m^* T \left(\frac{\pi}{3n}\right)^{2/3},$$

where k_B is the Boltzmann constant, m^* is the carrier's effective mass, n is the electron concentration, and T is the absolute temperature.

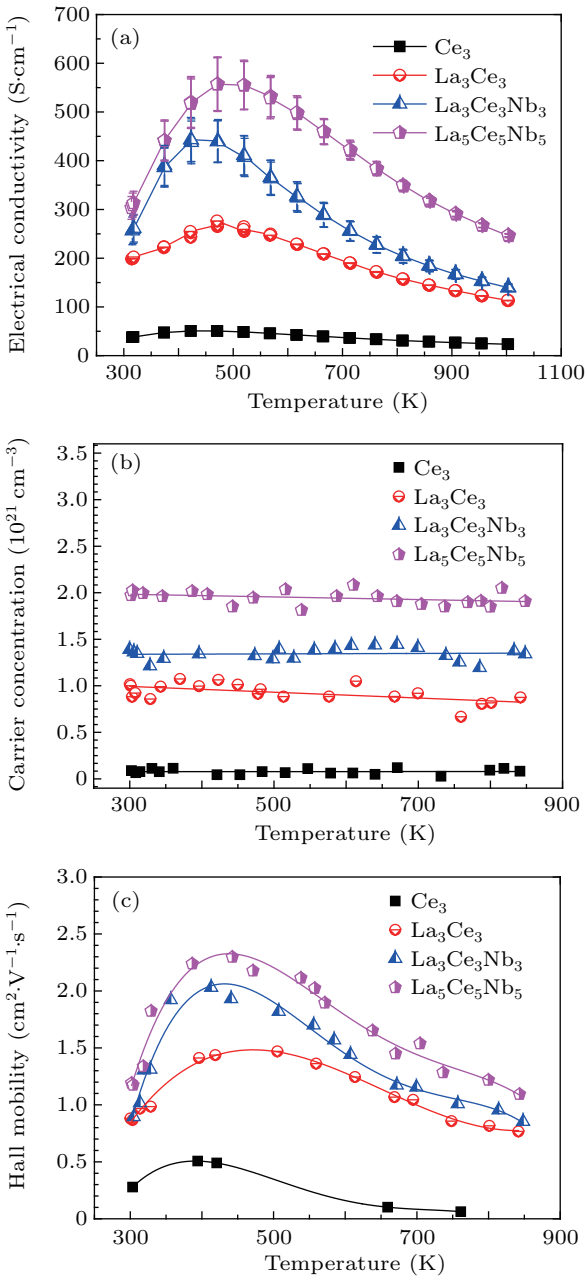


Fig. 8. Temperature-dependent electrical conductivity (a), carrier concentration (b), and mobility (c) of La–Ce–Nb doped $SrTiO_3$.

The Seebeck coefficient only slightly varied between samples La_3Ce_3 and $La_3Ce_3Nb_3$, even though sample $La_3Ce_3Nb_3$ contained more dopant (3-mol% Nb). This indicates that the enhancement effect of Nb on the effective mass produced a large Seebeck coefficient.[39] As shown in Fig. 10(a), the maximum power factor of 1.6 $mW \cdot m^{-1} \cdot K^2$

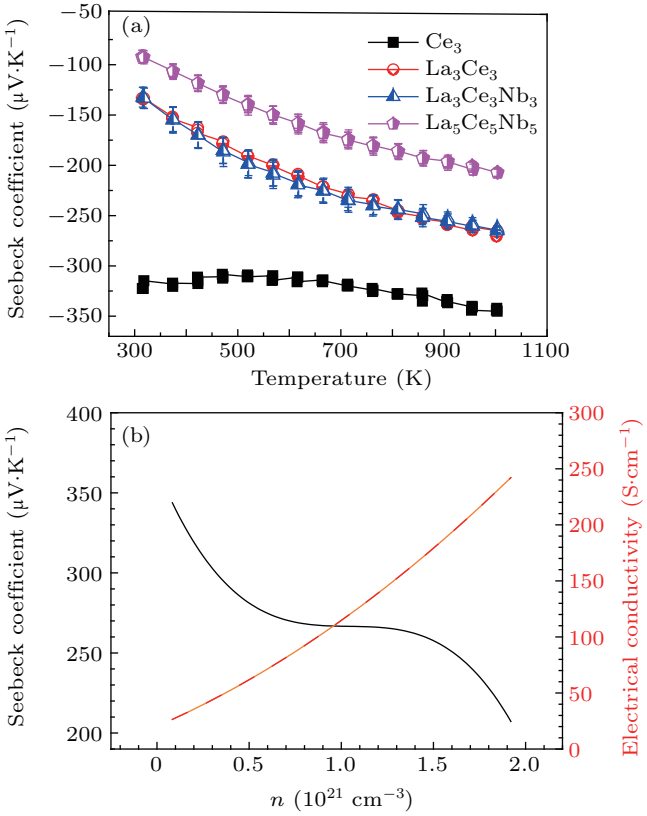


Fig. 9. Variation of the (a) Seebeck coefficient as a function of temperature, and (b) Seebeck coefficient together with electrical conductivity as a function of carrier concentration.

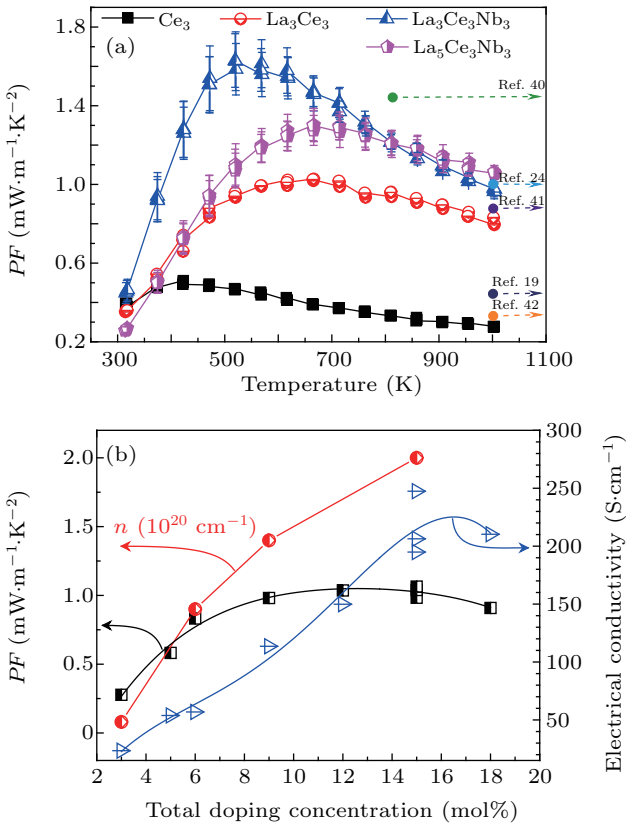


Fig. 10. Variation of (a) the power factor PF as a function of temperature together with PF reported previously, and (b) PF, carrier concentration, and electrical conductivity as a function of doping concentration.

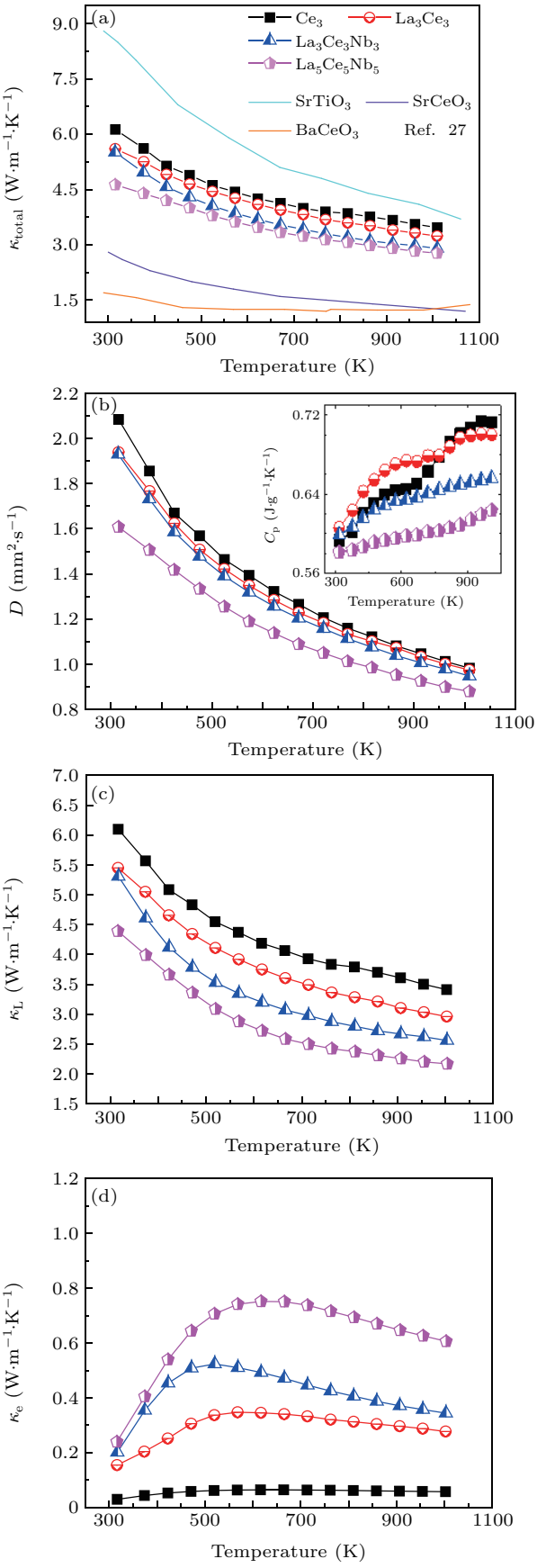


Fig. 11. Temperature dependence of (a) total thermal conductivity (κ_{total}), (b) thermal diffusivity (D) and specific heat (inset), (c) lattice thermal conductivity (κ_L), and (d) electrical thermal conductivity (κ_e) for present study together with thermal conductivity of $SrTiO_3$, $SrCeO_3$, and $BaCeO_3$ from Ref. [27].

was obtained for $La_3Ce_3Nb_3$ at 529 K, which decreased to 0.96 $mW{\cdot}m^{-1}{\cdot}K^2$ when the temperature increased to 1000 K. At 1000 K, sample $La_5Ce_5Nb_5$ showed the largest PF of 1.1 $mW{\cdot}m^{-1}{\cdot}K^2$, due to its high electrical conductivity, arising from its high carrier concentration and large carrier mobility. The PF values of this work are not significantly different from those of Nb and La-doped $SrTiO_3$ previously reported,[19,24,40–42] indicating that Ce did not significantly affect the PF. Because heavy doping promotes second phase precipitation,[17,26,33] the electrical conductivity decreased as the dopant ratio increased to over 15 mol%. This reduced the PF, as shown in Fig. 10(b). The doping concentration dependence on carrier concentration measured from 3 mol% to 15 mol% varied nonlinearly, which again demonstrates that the second phase increased with increasing doping concentration (Fig. 10(b)).

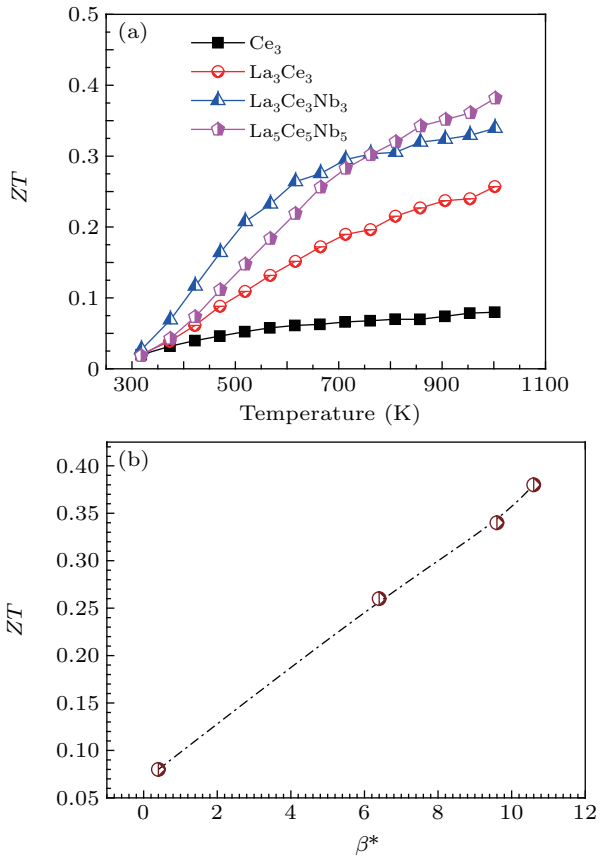


Fig. 12. The ZT as a function of (a) temperature and (b) β^* factor.

Figure 11 shows the temperature dependence of the thermal transport properties. The total thermal conductivity decreased to a minimum of 2.77 $W{\cdot}m^{-1}{\cdot}K^{-1}$ upon increasing the doping concentration in $La_5Ce_5Nb_5$. Although the value is still larger than that of $SrCeO_3$, and $BaCeO_3$, but lower than pure or La–Nb doped $SrTiO_3$,[17,26] suggesting that the Ce reduced the thermal conductivity. Such a low thermal conductivity may be related to the multiscale architecture with three dopants, nano-inclusions and nano/micro-sized grains.[43] The thermal diffusivity and lattice thermal

conductivity showed the same trend as κ_{total}, suggesting that the two factors were dominant for κ_{total}. Compared with κ_{total}, κ_{L} showed a greater decrease as the doping concentration increased, implying that the dopant, lattice distortion, and multi-scale interfaces produced a strong phonon scattering. The low lattice thermal conductivity and relatively large effective mass, together with a higher carrier mobility, produced a large $\beta^* = \mu(m^*/m)^{3/2}/\kappa_{\text{L}}$, which increased with increasing doping concentration up to 15 mol%. The ZT value increased with the increasing β^* factor, leading to a maximum ZT of around 0.38 at 1000 K with a maximum β^* factor of 10.6 in the $La_5Ce_5Nb_5$ sample (Fig. 12).

4. Conclusion

In this work, we investigated the microstructure and thermoelectric properties of La, Ce, and Nb-doped $SrTiO_3$. A powder with an average size of 20 nm was obtained using a hydrothermal method, and then La, Ce, and Nb were incorporated into $SrTiO_3$. The crystal grains grew abnormally during sintering and formed a complex microstructure. Co-doping with the three elements and the formation of multi-scale grain boundaries helped improve phonon scattering, which greatly decreased the lattice thermal conductivity to 2.17 $\text{W}\cdot\text{m}^{-1}\cdot\text{K}^{-1}$ at 1000 K. The maximum ZT of 0.38 is one of the highest values reported for $SrTiO_3$, which provides a reference for future research on n-type oxide thermoelectric materials.

Acknowledgements

Thanks Yanzhong Pei, Hongxia Liu from Tongji University for valuable discussion and support provided for the Hall effect measurements. Financial supports are given in the footnote on the first page.

References

[1] Lu X, Jiang P and Bao X 2019 *Nat. Commun.* **10** 138
[2] Okuda T, Nakanishi K, Miyasaka S and Tokura Y 2001 *Phys. Rev. B* **63** 113104
[3] Tritt T M and Subramanian M A 2011 *MRS Bull.* **31** 188
[4] Ohta H, Mizuno T, Zheng S, Kato T, Ikuhara Y, Abe K, Kumomi H, Nomura K and Hosono H 2012 *Adv. Mater.* **24** 740
[5] Xiao Y and Zhao L D 2020 *Science* **367** 1196
[6] Zhao L D, Lo S H, Zhang Y, Sun H, Tan G, Uher C, Wolverton C, Dravid V P and Kanatzidis M G 2014 *Nature* **508** 373
[7] Zhao W, Liu Z, Wei P, Zhang Q, Zhu W, Su X, Tang X, Yang J, Liu Y, Shi J, Chao Y, Lin S and Pei Y Z 2016 *Nat. Nano* **12** 55
[8] Wan C, Gu X, Dang F, Itoh T, Wang Y, Sasaki H, Kondo M, Koga K, Yabuki, Snyder G J, Yang R and Koumoto, K 2015 *Nat. Mater.* **14** 622
[9] Zheng Y, Liu C, Miao L, Li C, Huang R, Gao J, Wang X, Chen J, Zhou Y and Nishibori E 2019 *Nan. Energ.* **59** 311
[10] Minnich A J, Dresselhaus M S, Ren Z F and Chen G 2009 *Energ. Environ. Sci.* **2** 466
[11] Sales B C, Mandrus D and Williams R K 1996 *Science* **272** 1325
[12] Gao J, Miao L, Liu C, Wang X, Peng Y, Wei X, Zhou J, Chen Y, Hashimoto R, Asaka T and Koumoto K 2017 *J. Mate. Chem. A* **5** 24740
[13] Liu X and Padilla W J 2012 *Energ. Environ. Sci.* **5** 7188
[14] Li F, Li J F, Zhao L D, Xiang K, Liu Y, Zhang B P, Lin Y H, Nan C W and Zhu H M 2012 *Energ. Environ. Sci.* **5** 7188
[15] Ohta H, Kim S, Mune Y, Mizoguchi T, Nomura K, Ohta S, Nomura T, Nakanishi Y, Ikuhara Y, Hirano M, Hosono H and Koumoto K 2007 *Nat. Mater.* **6** 129
[16] Chen J, Chen H, Hao F, Ke X, Chen N, Yajima T, Jiang Y, Shi X, Zhou K, Döbeli M, Zhang, T, Ge B, Dong H, Zeng H, Wu W and Chen L 2017 *ACS Energ. Lett.* **2** 915
[17] Zhang B, Wang J, Zou T, Zhang S, Yaer X, Ding N, Liu C, Miao L, Li Y and Wu Y 2015 *J Mater. Chem. C* **3** 11406
[18] Muta H, Kurosaki K and Yamanaka S 2003 *J. Alloy. Compd.* **350** 292
[19] Lu Z, Zhang H, Lei W, Sinclair D C and Reaney I M 2016 *Chem. Mater.* **28** 925
[20] Srivastava D, Norman C, Azough F, Schäfer M C, Guilmeau E, Kepaptsoglou D, Ramasse Q M, Nicotra G and Freer R 2016 *Physl. Chem. Chem. Phys.* **18** 26475
[21] Ohta S, Nomura T, Ohta H and Koumoto K 2005 *J. Appl. Phys.* **97** 034106
[22] Abutaha A I, Kumar S R, Li K, Dehkordi A M, Tritt T M and Alshareef H N 2015 *Chem. Mater.* **27** 2165
[23] Yu C, Scullin M L, Huijben M, Ramesh R and Majumdar A 2008 *Appl. Phys. Lett.* **92** 191911
[24] Park K, Son J S, Woo S I, Shin K, Oh M W, Park S D and Hyeon T 2014 *J. Mater. Chem. A* **2** 4217
[25] Wang N, Chen H, He H, Norimatsu W, Kusunoki M and Koumoto K 2013 *Sci. Rep.* **3** 3449
[26] Wang J, Zhang B Y, Kang H J, Li Y, Yaer X, Li J F, Tan Q, Zhang S, Fan G H, Liu C Y, Miao L, Nan D, Wang T M and Zhao L D 2017 *Nan. Energ.* **35** 387
[27] Yamanaka S, Kurosaki K, Maekawa T, Matsuda T, Kobayashi S I and Uno M 2005 *J. Nucl. Mater.* **344** 61
[28] Liu C, Miao L, Hu D L, Huang R, Fisher C, Tanemura S and Gu H 2013 *Phys. Rev. B* **88** 205201
[29] Zhao K, Zhu C, Qiu P, Blichfeld A B, Eikeland E, Ren D, Iversen B B, Xu F, Shi X and Chen L 2017 *Nan. Energ.* **42** 43
[30] Yamasaka S, Nakamura Y, Ueda T, Takeuchi S and Sakai A 2015 *Sci. Rep.* **5** 14490
[31] Mao J, Liu Z, Zhou J, Zhu H, Zhang Q, Chen G and Ren Z F 2018 *Adv. Phys.* **67** 69
[32] Li Y, Hou Q Y, Wang X H, Kang H J, Yaer X, Li J B, Wang T M, Miao L and Wang J 2019 *J. Mater. Chem. A* **7** 236
[33] Li J B, Wang J, Li J F, Li Y, Yang H, Yu H Y, Ma X B, Yaer X, Liu L and Miao L J 2018 *Mater. Chem. C* **6** 7594
[34] Ohta S, Ohta H and Koumoto K 2006 *J. Ceram. Soc. Jpn* **114** 102
[35] Harada S, Tanaka K and Inui H 2010 *J. Appl. Phys.* **108** 083703
[36] Portehault D, Maneeratana V, Candolfi C, Oeschler N, Veremchuk I, Grin Y, Sanchez C and Antonietti M 2011 *ACS Nano* **5** 9052
[37] Liu C, Miao L, Zhou J, Huang R, Fisher C A and Tanemura S 2013 *J. Phys. Chem. C* **117** 11487
[38] He Y, Lu P, Shi X, Xu F, Zhang T, Snyder G J, Uher C and Chen L U 2015 *Adv. Mater.* **27** 3639
[39] Ohta S, Nomura T, Ohta H, Hirano M, Hosono H and Koumoto K 2005 *Appl. Phys. Lett.* **87** 092108
[40] Huang J L, Yan P, Liu Y P, Xing J J, Gu H, Fan Y C and Jiang W 2020 *Appl. Mater. Inter.* **17** 108
[41] Wang K X, Wang J, Li Y, Zou T, Wang X H, Li J B, Cao Z, Shi W J and Yaer X 2018 *Chin. Phys. B* **27** 048401
[42] Yue L, Colin N, Deepanshu S, Feridoon A, Li W, Mark R, Kevin S, Robert F and Ian A K 2015 *Appl. Mater. Inter.* **58** 136
[43] Biswas K, He J Q, Blum I D, Wu C I, Hogan T P, Seidman D N, Dravid V P and Kanatzidis M G 2012 *Nature* **489** 414